

# Overcoming Space-Charge Effect for Efficient Thick-Film Non-Fullerene Organic Solar Cells

Guichuan Zhang, Ruoxi Xia, Zhen Chen, Jingyang Xiao, Xuenan Zhao, Shiyuan Liu, Hin-Lap Yip,\* and Yong Cao

Organic solar cells (OSCs) containing non-fullerene acceptors have realized high power conversion efficiency (PCE) up to 14%. However, most of these high-performance non-fullerene OSCs have been reported with optimal active layer thickness of about 100 nm, mainly due to the low electron mobility ( $\approx 10^{-4}$ – $10^{-5}$  cm<sup>2</sup> V<sup>-1</sup> s<sup>-1</sup>) of non-fullerene acceptors, which are not suitable for roll-to-roll large-scale processing. In this work, an efficient non-fullerene OSC based on poly[(5,6-difluoro-2,1,3-benzothiadiazol-4,7-diyl)-alt-(3,3''-di(2-octyldodecyl)-2,2';5',2'';5'',2'''-quaterthiophen-5,5'''-diyl)] (PffBT4T-2OD):EH-IDTBR (consists of electron-rich indaceno[1,2-b:5,6-b']dithiophene as the central unit and an electron-deficient 5,6-benzo[c][1,2,5]thiadiazole unit flanked with rhodanine as the peripheral group) with thickness-independent PCE (maintaining a PCE of 9.1% with an active layer thickness of 300 nm) is presented by optimizing device architectures to overcome the space-charge effects. Optical modeling reveals that most of the incident light is absorbed near the transparent electrode side in thick-film devices. The transport distance of electrons with lower mobility will therefore be shortened when using inverted device architecture, in which most of the excitons are generated close to the cathode side and therefore substantially reduces the accumulation of electrons in the device. As a result, an efficient thick-film non-fullerene OSC is realized. These results provide important guidelines for the development of more efficient thick-film non-fullerene OSCs.

Over the last few years, advances in organic solar cells (OSCs) have progressed dramatically due to the rapid development of

Dr. G. Zhang, Prof. H.-L. Yip  
Innovation Center of Printed Photovoltaics  
South China Institute of Collaborative Innovation  
Dongguan 523808, P. R. China  
E-mail: msangusyip@scut.edu.cn

Dr. G. Zhang, R. Xia, Z. Chen, J. Xiao, Prof. H.-L. Yip, Prof. Y. Cao  
State Key Laboratory of Luminescent Materials and Devices  
Institute of Polymer Optoelectronic Materials and Devices  
School of Materials Science and Engineering  
South China University of Technology  
381 Wushan Road, Guangzhou 510640, P. R. China

X. Zhao, Prof. S. Liu  
State Key Laboratory of Digital Manufacturing Equipment and Technology  
Huazhong University of Science and Technology  
Wuhan 430074, P. R. China

Prof. S. Liu  
Wuhan Eoptics Technology Co. Ltd.  
Wuhan, Hubei 430075, P. R. China

The ORCID identification number(s) for the author(s) of this article can be found under <https://doi.org/10.1002/aenm.201801609>.

DOI: 10.1002/aenm.201801609

non-fullerene acceptors (NFAs), which exhibit large tunability in energy levels and absorption spectra, providing more opportunities for the achievement of high-performance devices.<sup>[1–3]</sup> Benefiting from novel acceptor or donor material design<sup>[4–8]</sup> and device engineering,<sup>[9–11]</sup> the power conversion efficiencies (PCEs) of non-fullerene OSCs were dramatically increased from 6% to 14% in just a few years.<sup>[8,12]</sup> These novel NFAs are small molecules or polymers based on fused rings, such as perylene diimide,<sup>[13–16]</sup> naphthalene diimide,<sup>[17,18]</sup> and indacenodithiophene (IDT).<sup>[5,19–21]</sup> Among them, IDT-based small molecules are the most widely studied NFAs and have the best potential to achieve high-performance devices.<sup>[5,22–29]</sup>

However, most studies on the NFA-based OSCs were focused on boosting the PCE; fewer concentrated on issues related to future industrialization, including operation stability<sup>[30]</sup> and technologies for achieving efficient thick-film devices that are required for high speed, large-area manufacturing process.<sup>[31]</sup> It is well known that most IDT-based NFAs exhibit an

electron mobility of about  $10^{-4}$ – $10^{-5}$  cm<sup>2</sup> V<sup>-1</sup> s<sup>-1</sup>, which is lower than that of fullerene acceptors ( $\approx 10^{-3}$  cm<sup>2</sup> V<sup>-1</sup> s<sup>-1</sup>); this imbalance in charge transport properties limits the optimal active layer thickness of these devices to about 100 nm. Only a few studies reported relatively efficient thick-film non-fullerene OSCs based on exceptional acceptors with improved mobility,<sup>[20,32–34]</sup> and there remains a lack of more in-depth studies and strategies to achieve efficient thick-film non-fullerene OSCs.

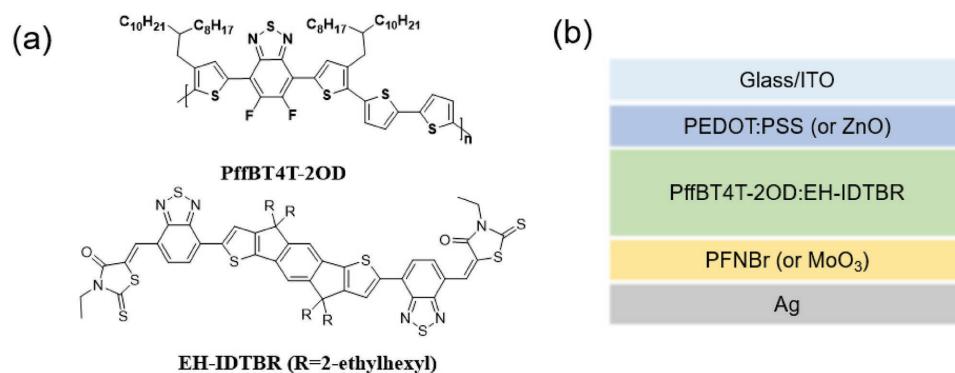
In this work, we demonstrate an effective strategy to realize efficient thick-film non-fullerene OSCs by overcoming the space-charge effects. Blends of a donor poly[(5,6-difluoro-2,1,3-benzothiadiazol-4,7-diyl)-alt-(3,3''-di(2-octyldodecyl)-2,2';5',2'';5'',2'''-quaterthiophen-5,5'''-diyl)] (PffBT4T-2OD)<sup>[35]</sup> and a non-fullerene small molecule acceptor EH-IDTBR (consists of electron-rich indaceno[1,2-b:5,6-b']dithiophene as the central unit and an electron-deficient 5,6-benzo[c][1,2,5]thiadiazole unit flanked with rhodanine as the peripheral group)<sup>[21]</sup> are chosen as the active layer because of their excellent device stability and these may be good candidates for commercial OSC applications.<sup>[36]</sup> Furthermore, PffBT4T-2OD can offer highly efficient thick-film OSCs with blends of [6,6]-phenyl-C61-butyric acid methyl ester (PCBM), which

can be attributed to the extremely high hole mobility of PffBT4T-2OD (about  $10^{-3}$ – $10^{-2}$   $\text{cm}^2 \text{V}^{-1} \text{s}^{-1}$ ).<sup>[35]</sup> It is thus possible for holes to freely transport through the whole thick-film devices based on PffBT4T-2OD:EH-IDTBR. First, PffBT4T-2OD:EH-IDTBR-based OSCs with various active layer thicknesses are fabricated in conventional device architecture, and we found that thick-film conventional devices present serious space-charge effects that dramatically decrease the PCE. This comes from the unbalanced transportation of holes and electrons in the conventional thick-film devices caused by unbalanced hole and electron mobilities, as EH-IDTBR shows a low electron mobility of about  $10^{-5}$   $\text{cm}^2 \text{V}^{-1} \text{s}^{-1}$ . Furthermore, optical modeling reveals that most of the incident light is absorbed near the transparent electrode side in both conventional and inverted thick-film devices. This means that the transport distance of electrons to the cathode is much longer than that of holes to the anode in conventional thick-film devices, which will exaggerate the space-charge effects. However, the overall transport distance of electrons will be shortened when using inverted device architecture, which greatly reduces the accumulation of electrons in the thick-film devices. As a result, PffBT4T-2OD:EH-IDTBR-based OSCs fabricated in inverted architecture showed thickness-independent PCE with a best PCE of 9.1% even when the active layer thickness increased to 300 nm. These results can provide important guidelines for the development of more efficient thick-film non-fullerene OSCs.

**Scheme 1a** shows the chemical structures of PffBT4T-2OD and EH-IDTBR. First, we fabricated PffBT4T-2OD:EH-IDTBR-based OSCs with active layer thickness varying from 100 to 300 nm using conventional device architecture, ITO/PEDOT:PSS/PffBT4T-2OD:EH-IDTBR/Poly[(9,9-bis(3'-(*N,N*-dimethyl)-*N*-ethylammonium)-propyl)-2,7-fluorene]-alt-2,7-(9,9-dioctylfluorene)] Dibromide (PFNBr)/Ag (**Scheme 1b**). **Figure 1a** shows the current-density/voltage (*J*–*V*) curves of the conventional devices with the best photovoltaic performance. The detailed photovoltaic parameters of these devices are summarized in **Table 1**. The devices with an active layer thickness of 100 nm show the best PCE, 9.4%, with a short-circuit current density ( $J_{\text{sc}}$ ) of 13.6  $\text{mA cm}^{-2}$ , an open-circuit voltage ( $V_{\text{oc}}$ ) of 1.04 V, and a fill factor (FF) of 66.1%. However, the PCE drops rapidly as the active layer thickness increases, with a PCE of only 6.8% when the thickness is 300 nm. This mainly results from

the significant decrease of FF to 49.1% with slight changes of  $V_{\text{oc}}$  and  $J_{\text{sc}}$  (**Figure 1b**). The result of subtle change in  $J_{\text{sc}}$  is differed from the efficient thick-film fullerene-based OSCs, for which  $J_{\text{sc}}$  typically enhances with increasing active layer thickness.<sup>[37,38]</sup> In our case, the  $J_{\text{sc}}$  of PffBT4T-2OD:EH-IDTBR-based conventional OSCs increases slightly from 13.6 to 14.1  $\text{mA cm}^{-2}$  when the thickness increases from 100 to 200 nm but drops to 13.7  $\text{mA cm}^{-2}$  when it increases to 300 nm, which is consistent with the  $J_{\text{sc}}$  calculated from the external quantum efficiency (EQE) spectra with an error of about <5% (**Table 1** and **Figure 1c**). Thus, PffBT4T-2OD:EH-IDTBR-based conventional OSCs are not able to realize efficient thick-film devices, which is further confirmed by measuring the characteristics of photocurrent density ( $J_{\text{ph}}$ ) versus effective voltage ( $V_{\text{effect}}$ ) to investigate the charge generation, dissociation, and extraction properties.<sup>[39]</sup> Generally, all of the photogenerated excitons will be dissociated into free charges and collected by electrodes at high  $V_{\text{effect}}$  (in this case, 3 V). Therefore, saturation current density ( $J_{\text{sat}}$ ) and charge dissociation probabilities  $P(E,T)$  ( $J_{\text{ph}}/J_{\text{sat}}$ ) at different  $V_{\text{effect}}$  can be extracted from the  $J_{\text{ph}}-V_{\text{effect}}$  curves. From **Figure 1d**, it can be intuitively found that  $J_{\text{ph}}$  continues to decrease as the thickness increases at the same  $V_{\text{effect}}$  in the low  $V_{\text{effect}}$  region (<1 V), which is consistent with the variation in FF. Moreover, under the short-circuit condition, the  $P(E,T)$  values are 88.6%, 80.4%, and 74.1% for conventional devices with active layer thicknesses of 100, 200, and 300 nm, respectively, which indicates that the devices with a thicker active layer are less efficient in charge dissociation and extraction. However, all the slopes of logarithmic  $J_{\text{sc}}$  versus logarithmic light intensity for the conventional devices with various thickness are near 1 (**Figure S1a**, Supporting Information), which suggests that the bimolecular recombination is very weak in these devices. The slopes of  $V_{\text{oc}}$  versus the natural logarithm of light intensity for these devices remain at  $\approx 1.20$   $\text{kT q}^{-1}$  with increasing active layer thickness (**Figure S1b**, Supporting Information), indicating less or even unchanged monomolecular recombination.<sup>[40]</sup>

It is known that high charge mobility is usually needed for efficient thick-film OSCs.<sup>[35,41]</sup> Therefore, to further investigate the origin of the lower performance for conventional devices with a thicker active layer, the electron and hole mobilities of PffBT4T-2OD:EH-IDTBR are determined using the space-charge limited current (SCLC) method and are calculated to be  $\approx 10^{-5}$  and  $10^{-3}$   $\text{cm}^2 \text{V}^{-1} \text{s}^{-1}$ , respectively (**Figure S2**, Supporting Information).



**Scheme 1.** a) Chemical structure of PffBT4T-2OD and non-fullerene acceptor EH-IDTBR. b) Architectures of conventional (or inverted) devices based on PffBT4T-2OD:EH-IDTBR.

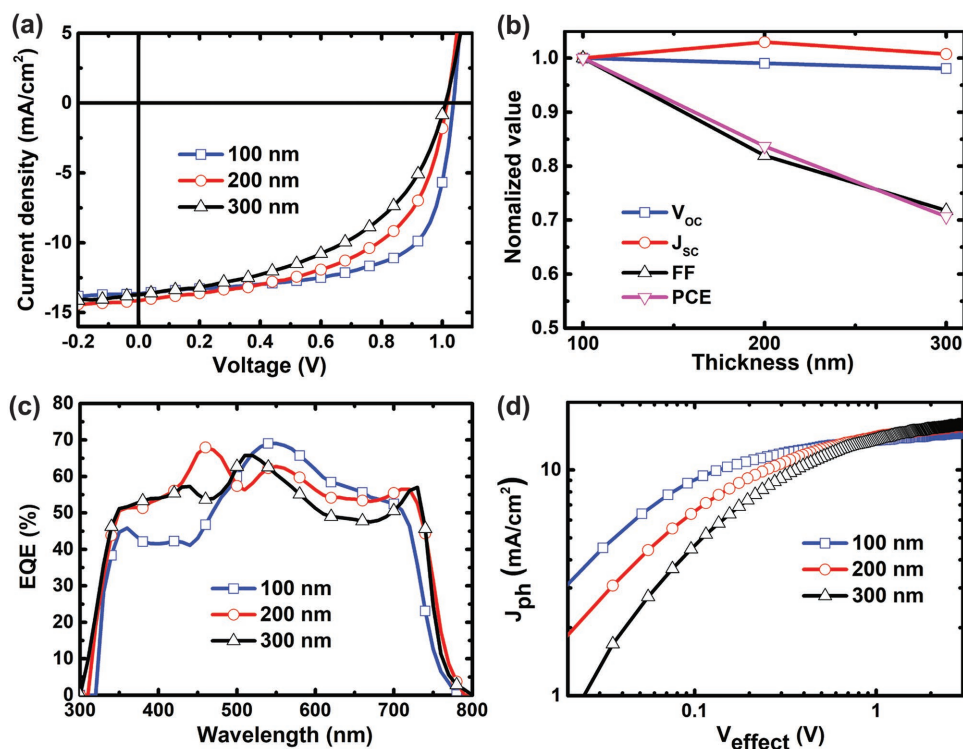


**Figure 1.** a)  $J$ - $V$  curves, b) normalized value of all photovoltaic parameters, c) EQE spectra, and d)  $J_{ph}$  versus  $V_{effect}$  curves of PffBT4T-2OD:EH-IDTBR-based OSCs with various active layer thicknesses using conventional device architecture.

The unbalanced charge transport property facilitates the formation of space-charge, especially in thick-film devices, which seriously limits the performance of the devices.<sup>[42,43]</sup>

The formation of the space-charge can be studied by measuring the characteristics of  $J_{ph}$  versus  $V_{effect}$  under various light intensities.<sup>[42]</sup> First, the space-charge limited (SCL) photocurrent shows square-root dependence on the  $V_{effect}$ . For the conventional device with active layer thickness of 100 nm, the square-root region is very small and has a  $V_{effect}$  below 0.1 V and it gradually disappears as the light intensity decreases (Figure 2a), suggesting a weak space-charge formation, which is consistent with the good performance of the device with high FF. For the device with active layer thickness of 300 nm, obvious square-root region is shown between 0.1 and 0.4 V under light intensity of  $\approx 1$  sun ( $100 \text{ mW cm}^{-2}$ ) and it only slightly moves towards lower  $V_{effect}$  as the light intensity decreases (Figure 2b) instead of complete diminishment as shown in thin-film devices, indicating stronger space-charge formation in the thick-film devices. Moreover, the SCL photocurrent is expected to scale with a 0.75 power dependence on

light intensity.<sup>[42]</sup> In Figure 2c, the light-dependent  $J_{ph}$  under three different bias conditions including  $V_{effect} = 0.1$  V in the square-root region, short-circuit condition, and  $V_{effect} = 3$  V in the saturation region are extracted from Figure 2b and plotted based on a double logarithmic coordinate. The slope determined from the linear fit of the extracted data is 0.73 in the square-root region, which is another strong indication of the occurrence of an SCL photocurrent. The slope is determined to be near 1 under the short-circuit condition and in the saturation region, which is the same as the characteristics of  $J_{sc}$  versus the light intensity mentioned above. Another way to confirm the presence of space-charge is to consider the voltage  $V_{sat}$  at which  $J_{ph}$  switches from square-root dependence to the saturation region and  $V_{sat}$  scales with the square root of light intensity.<sup>[42]</sup> The  $V_{sat}$  is extracted from the crossover point of the square-root region and the extrapolated saturation region, as indicated by the arrow in Figure 2b. The  $V_{sat}$  versus light intensity is plotted in Figure 2d using the double logarithmic coordinate. A slope of 0.49 is found, which is in good agreement with the SCL prediction (of 0.5), further confirming that

**Table 1.** Photovoltaic parameters of PffBT4T-2OD:EH-IDTBR (1:1.5, w/w)-based OSCs with various active layer thicknesses using conventional device architecture.

Thickness [nm]	$V_{oc}$ [V] <sup>a)</sup>	$J_{sc}$ [ $\text{mA cm}^{-2}$ ] <sup>a)</sup>	FF [%] <sup>a)</sup>	PCE [%] <sup>a)</sup>	$J_{sc}$ [ $\text{mA cm}^{-2}$ ] <sup>b)</sup>
100	1.04 (1.03 $\pm$ 0.00)	13.6 (13.5 $\pm$ 0.1)	66.1 (65.9 $\pm$ 0.8)	9.4 (9.2 $\pm$ 0.2)	12.9
200	1.02 (1.02 $\pm$ 0.00)	14.1 (13.9 $\pm$ 0.1)	55.1 (54.0 $\pm$ 1.0)	7.9 (7.7 $\pm$ 0.2)	13.8
300	1.01 (1.01 $\pm$ 0.00)	13.7 (13.6 $\pm$ 0.1)	49.1 (47.3 $\pm$ 1.8)	6.8 (6.5 $\pm$ 0.3)	13.0

<sup>a)</sup>Statistical data obtained from over 10 devices shown in brackets; <sup>b)</sup>The  $J_{sc}$  integrated from the EQE spectrum.

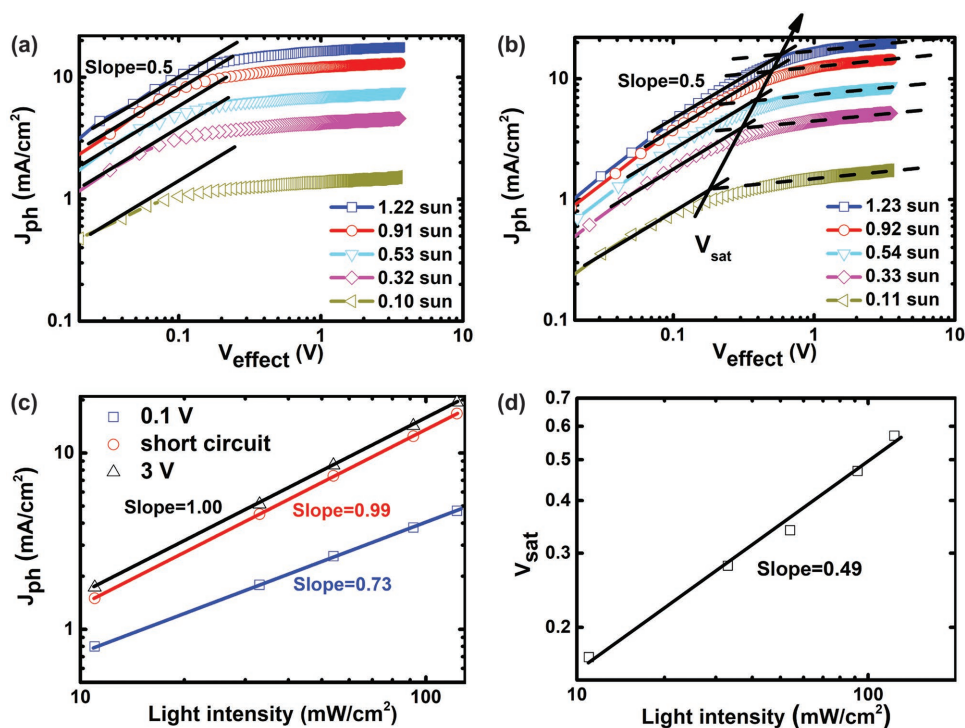


**Figure 2.**  $J_{ph}$  versus  $V_{effect}$  curves of PffBT4T-2OD:EH-IDTBR-based OSCs with active layer thicknesses of a) 100 nm and b) 300 nm using conventional device architecture. c)  $J_{ph}$  at various  $V_{effect}$  and d)  $V_{sat}$  versus light intensity extracted from (b).

the photocurrent of the thick-film device is mainly limited by the space-charge effects and therefore the FF of the device will also be strongly limited,<sup>[42]</sup> leading to the poor performance of PffBT4T-2OD:EH-IDTBR-based conventional thick-film OSCs.

In order to overcome the space-charge effects for efficient thick-film OSCs, the extraction rate of charge carrier with lower mobility, which is electron in this case, should be improved; this can be realized by increasing the electron mobility or shortening the transport distance of the electrons to the cathode. In general, carrier mobility is governed by the intrinsic charge transport property of the organic semiconductor; improving electron mobility therefore requires the design and synthesis of new acceptors, which indeed is very challenging to accomplish for NFAs. A

more affordable way to overcome the space-charge effects is by shortening the electron transport distance, which can be achieved by altering the device architecture so as to generate a more favorable exciton generation profile in the bulk-heterojunction (BHJ) film to reduce the overall electron transport distance to the cathode. The analysis of the exciton generation profile (or photon absorption rate profile) within different component layers are therefore performed using transfer matrix optical model<sup>[44,45]</sup> and the results for PffBT4T-2OD:EH-IDTBR-based OSCs with active layer thickness of 100, 200, and 300 nm using conventional and inverted device architectures are summarized in Figure S3 (Supporting Information) and **Figure 3**. As shown in those figures, the photon absorption profiles are relatively uniform

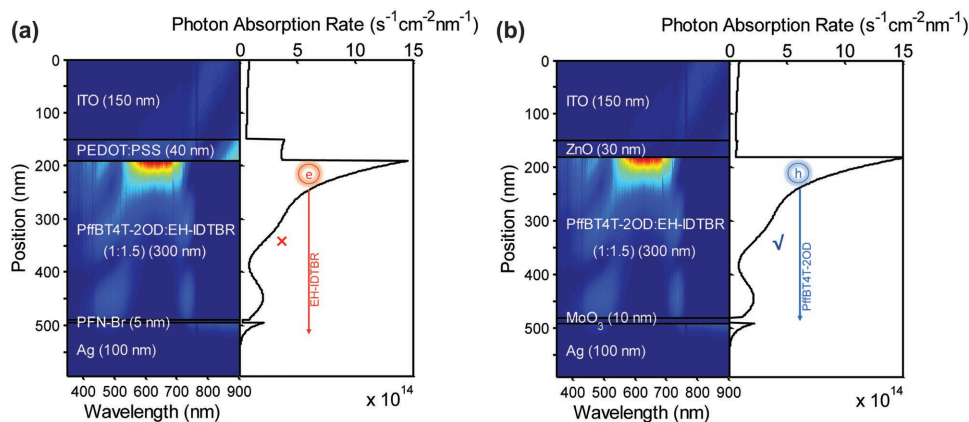


**Figure 3.** Simulated photoabsorption rate in PffBT4T-2OD:EH-IDTBR-based OSCs with active layer thicknesses of 300 nm using a) conventional and b) inverted device architecture.

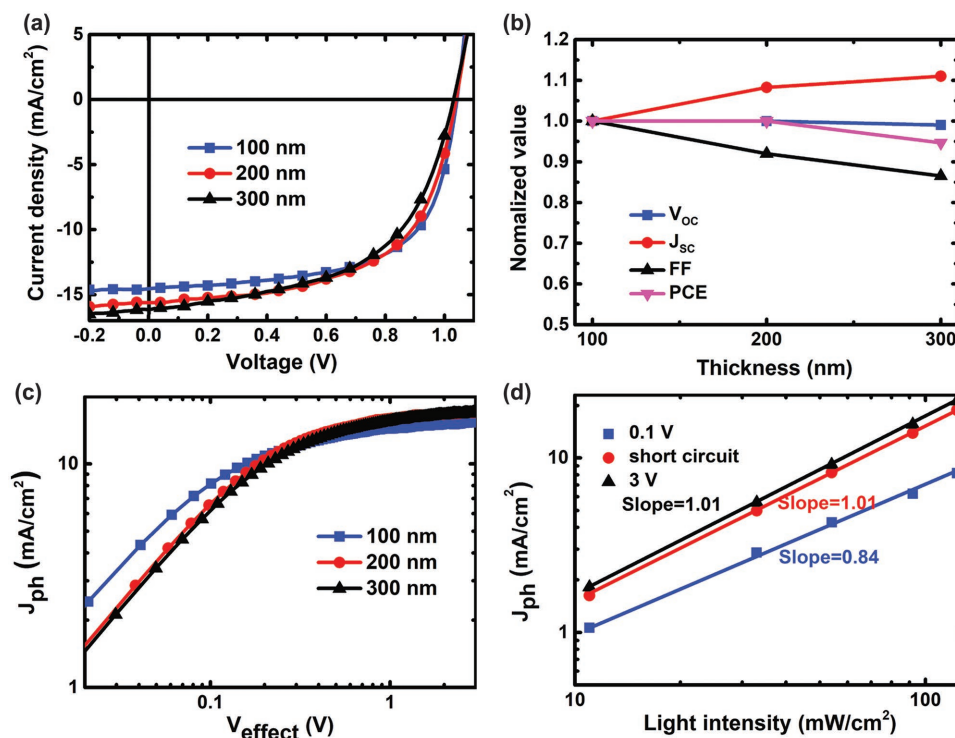


**Figure 4.** a)  $J$ - $V$  curves, b) normalized value of all photovoltaic parameters, and c)  $J_{ph}$  versus  $V_{effect}$  curves of PffBT4T-2OD:EH-IDTBR-based OSCs with various active layer thicknesses using inverted device architecture. d) Light intensity dependence of  $J_{ph}$  at various  $V_{effect}$  extracted from Figure S4d.

over the active layer region in thin-film (100 nm) devices, but most of the photons are absorbed near the transparent electrode side in thick-film (200 and 300 nm) devices, regardless of the device architectures. Assuming most of the photons absorbed in our optimized BHJ films can be effectively separated into free charges, the plots in Figure S3 (Supporting Information) and Figure 3 can then also be viewed as the charge generation profile within the devices. Therefore, it can be speculated that the generation of free charges (electrons and holes) are mainly concentrated near the transparent electrode side in thick-film devices. In such case, the transport distance for the two different types of carriers before reaching the corresponding electrodes is strongly dependent on the device architectures. In the thick-film device with conventional architecture (Figure 3a), most of the electrons need to transport a much longer distance to the cathode (through EH-IDTBR with lower mobility) and most of the holes only need to transport short distance to reach the anode (through PffBT4T-2OD with higher mobility), which will aggravate the space-charge effect as discussed above. However, in the thick-film device with inverted architecture (Figure 3b), the transport distance of most of the electrons to the cathode is much shorter than that of most of the holes transport to the anode, which can greatly facilitate electron extraction to mitigate the space-charge effect. Furthermore, most of the holes in the PffBT4T-2OD:EH-IDTBR system are supposed to be efficiently collected by the anode because PffBT4T-2OD exhibits very high mobility.<sup>[35]</sup> Therefore, PffBT4T-2OD:EH-IDTBR-based OSCs using inverted architecture are expected to realize efficient thick-film devices.

To verify the result obtained from optical modeling, we fabricated PffBT4T-2OD:EH-IDTBR-based OSCs with active layer

thicknesses ranging from 100 to 300 nm using inverted device architecture, ITO/ZnO/PffBT4T-2OD:EH-IDTBR/MoO<sub>3</sub>/Ag (Scheme 1b). Figure 4a shows the  $J$ - $V$  curves of the inverted devices with the best photovoltaic performance. The detailed photovoltaic parameters of these devices are summarized in Table 2. The devices with an active layer thickness of 100 nm show the best PCE of 9.5% with a  $J_{sc}$  of 14.5 mA cm<sup>-2</sup>, a  $V_{oc}$  of 1.04 V, and an FF of 63.0%, which is comparable to the conventional ones. However, the PCE remains at 9.5% when the active layer thickness increases to 200 nm; even when the thickness keeps increasing to 300 nm, the PCE remains at 9.1%. These results can be attributed to the enhanced  $J_{sc}$  and invaried  $V_{oc}$  with increasing active layer thickness, although there is a slight decrease in FF (Figure 4b). In contrast to the conventional devices in which  $J_{sc}$  changes little with increasing active layer thickness, the  $J_{sc}$  of inverted devices increases further from 14.5 to 16.1 mA cm<sup>-2</sup> when the thickness increases from 100 to 300 nm, which is consistent with the  $J_{sc}$  calculated from the EQE spectra with an error <5% (Table 2; Figure S4a, Supporting Information). The characteristics of  $J_{ph}$  versus  $V_{effect}$  for the inverted devices are also measured to investigate the charge generation, dissociation, and extraction properties. From Figure 4c, unlike the conventional devices in which  $J_{ph}$  decreases to a low value in the low  $V_{effect}$  region (<1 V) when the active layer thickness increases, the  $J_{ph}$  of inverted devices only slightly decreases at the same  $V_{effect}$  in a lower voltage region (<0.3 V) with increasing active layer thickness, which is consistent with the trend of variation in FF. Quantitatively, the  $P(E,T)$  values under the short-circuit condition are obtained as 88.1%, 85.7%, and 82.9% for the inverted devices with active layer

**Table 2.** Photovoltaic parameters of PffBT4T-2OD:EH-IDTBR (1:1.5, w/w)-based OSCs with various active layer thicknesses using inverted device architecture.

Thickness [nm]	$V_{oc}$ [V] <sup>a)</sup>	$J_{sc}$ [mA cm <sup>-2</sup> ] <sup>a)</sup>	FF [%] <sup>a)</sup>	PCE [%] <sup>a)</sup>	$J_{sc}$ [mA cm <sup>-2</sup> ] <sup>b)</sup>
100	1.04 (1.04 ± 0.00)	14.5 (14.5 ± 0.1)	63.0 (62.4 ± 0.5)	9.5 (9.4 ± 0.1)	13.9
200	1.04 (1.04 ± 0.00)	15.6 (15.7 ± 0.1)	58.5 (57.4 ± 0.7)	9.5 (9.4 ± 0.1)	14.9
300	1.03 (1.03 ± 0.00)	16.1 (16.0 ± 0.3)	54.5 (54.0 ± 1.1)	9.1 (8.9 ± 0.2)	15.6

<sup>a)</sup>Statistical data obtained from over 10 devices shown in brackets; <sup>b)</sup>The  $J_{sc}$  integrated from the EQE spectrum.

thicknesses of 100, 200, and 300 nm, respectively, indicating that the inverted thick-film devices are more efficient in charge dissociation and extraction than the conventional ones. Moreover, all of the slopes of logarithmic  $J_{sc}$  versus logarithmic light intensity for the inverted devices with various thicknesses are near 1 (Figure S4b, Supporting Information), which suggests that bimolecular recombination is very weak in these devices. Therefore, the performance of these efficient thick-film devices should not be limited by the space-charge effect.

We experimentally prove the weaker space-charge effect by measuring the characteristics of  $J_{ph}$  versus  $V_{effect}$  of the inverted devices under various light intensities. The inverted thin-film (100 nm) device exhibits a similar characteristic with the conventional thin-film one (Figure 2a): the square-root region is very small and presents at  $V_{effect}$  below 0.1 V (Figure S4c, Supporting Information), suggesting a weak space-charge formation, which is revealed by the good performance of the device. For inverted thick-film (300 nm) devices, the square-root region is much smaller than the conventional thick-film ones (Figure 2b), which presents at  $V_{effect}$  below 0.2 V and gradually disappears with decreasing light intensity, indicating that space-charge effects are overcome in thick-film devices using inverted architecture. Furthermore, from Figure S4d (Supporting Information), we also extracted the  $J_{ph}$  at  $V_{effect} = 0.1$  V, short-circuit condition, and  $V_{effect} = 3$  V in the saturation region under various light intensities and replotted in the double logarithmic coordinate (Figure 4d) for a better evaluation of the space-charge effect. Under short-circuit condition or in the saturation region, the slopes determined from the linear fit to the extracted data are 1, the same as the characteristic of  $J_{sc}$  versus light intensity mentioned above. At  $V_{effect} = 0.1$  V, the slope determined from the linear fit to the extracted data is 0.84, which is much higher than the SCL prediction (of 0.75), which further confirms that less space-charge is formed in these devices. Therefore, guiding by optical modeling, we experimentally prove that space-charge effects can be overcome by using inverted device architecture in PffBT4T-2OD:EH-IDTBR-based thick-film OSCs.

In summary, we successfully developed an efficient thick-film OSC based on the PffBT4T-2OD:EH-IDTBR non-fullerene system by overcoming the space-charge effects. PffBT4T-2OD:EH-IDTBR-based conventional OSCs show rapidly decreasing performance with increasing active layer thickness due to the formation of space-charge caused by unbalanced charge transport ability and charge transport distance determined by the SCLC method and optical modeling. However, the space-charge effect is greatly overcome by shortening the transport distance of electrons for efficient charge collection when using inverted device architecture, which greatly reduces

the accumulation of electrons in the device. As a result, an efficient non-fullerene OSC with PCE less dependent on the BHJ thickness is presented, maintaining a PCE of 9.1% even with an active layer thickness of 300 nm. Our results thus show that optimizing device architecture is a simple and effective strategy to realize efficient thick-film non-fullerene OSCs by overcoming the space-charge effects, and these findings can provide useful guidelines for the development of more efficient thick-film OSCs, which are important to realize roll-to-roll printed OSCs in the future.

## Experimental Section

*Fabrication and Characterization of OSCs:* PffBT4T-2OD and EH-IDTBR were purchased from 1-Material, Inc.; PFNBr was purchased from Solarmer, Inc. The ITO glass substrates were cleaned sequentially under sonication with acetone, detergent, deionized water, and isopropyl alcohol and then dried at 60 °C in a baking oven overnight, followed by a 4-min oxygen plasma treatment. For conventional devices, a PEDOT:PSS layer (≈40 nm) was spun on ITO substrates and dried in air at 150 °C for 15 min. All substrates were then transferred to a glovebox under nitrogen ( $N_2$ ) for the following deposition of active layers. The solutions of PffBT4T-2OD:EH-IDTBR (1:1.5, w/w) were prepared in o-xylene and stirred on a hot plate at 100 °C over 3 h. Active layers were spin-coated from hot active layer solutions on the pretreated substrates to obtain the required thicknesses by changing the concentration of the active layer solutions or the spinning rate. The film thicknesses were determined with a Dektak 150 stylus surface profiling system (Veeco). The active layer films were then annealed at 100 °C for 5 min before the next procedure. A 5-nm PFNBr cathode interfacial layer was then spin-coated from PFNBr methanol solution at a concentration of 0.5 mg mL<sup>-1</sup> at 2000 rpm for 30 s on active layers, and the samples were transferred to the vacuum chamber. At a vacuum level of  $1 \times 10^{-7}$  Torr, 100 nm of Ag was thermally deposited as the top electrode through a shadow mask. For inverted devices, a ZnO electron transport layer was prepared by spin-coating at 5000 rpm for 30 s from a ZnO precursor solution (diethyl zinc) on ITO substrates. The active layers were deposited as mentioned above; at a vacuum level of  $1 \times 10^{-7}$  Torr, a thin layer (10 nm) of MoO<sub>3</sub> was then thermally deposited as the anode interlayer, followed by thermal deposition of 100 nm of Ag as the top electrode through a shadow mask. The active area of all devices was 0.08 cm<sup>2</sup>. The  $J$ - $V$  curves were measured on a computer-controlled Keithley 2400 source meter under 1 sun, the AM 1.5 G spectra was from a class solar simulator (Enlitech, Taiwan), and the light intensity was 100 mW cm<sup>-2</sup> as calibrated by a China General Certification Center-certified reference monocrystal silicon cell (Enlitech). Before the  $J$ - $V$  test, a physical mask with an aperture with precise area of 0.04 cm<sup>2</sup> was used to define the device area. The measurements of  $J_{sc}$ ,  $V_{oc}$ , and  $J_{ph}$  versus  $V_{effect}$  under different light intensity were performed on the above system. The EQE spectra measurements were performed on a commercial EQE measurement system (QE-R3011, Enlitech).

*Fabrication and Characterization of Electron- and Hole-Only Devices:* Devices were fabricated to measure the electron and hole mobilities by

using the SCLC method. The electron-only device structure was ITO/Al/active layer/Ca/Al; the hole-only device structure was ITO/PEDOT:PSS/active layer/MoO<sub>3</sub>/Ag. The mobility was determined by fitting the dark current to the model of a single-carrier SCLC, which is described by the equation  $J = (9/8)\epsilon_0\epsilon_r\mu((V^2)/(d^3))$ , where  $J$  is the current density,  $\mu$  is the zero-field mobility,  $\epsilon_0$  is the permittivity of free space,  $\epsilon_r$  is the relative permittivity of the material,  $d$  is the thickness of the active layers, and  $V$  is the effective voltage. The effective voltage was obtained by subtracting the built-in voltage ( $V_{bi}$ ) and the voltage drop ( $V_s$ ) from the series resistance of the whole device except for the active layers from the applied voltage ( $V_{app}$ ),  $V = V_{app} - V_{bi} - V_s$ . The mobility can be calculated from the slope of the  $J^{1/2}$ - $V$  curves.

**Optical Modeling:** The optical model was preformed based on the Transfer Matrix Formalism model. The optical parameters of  $n$  and  $k$  for different films were measured using a dual rotating-compensator Mueller matrix ellipsometer (ME-L ellipsometer, Wuhan Eoptics Technology Co., Wuhan, China), as described in detail in the reference.<sup>[43]</sup>

## Supporting Information

Supporting information is available from the Wiley Online Library or from the author.

## Acknowledgements

G.Z., R.X., Z.C., J.X., H.-L.Y., and Y.C., thank the Ministry of Science and Technology (Nos. 2017YFA0206600 and 2014CB643505), the National Natural Science Foundation of China (Nos. 21761132001, 91633301, 51573057), Science and Technology Program of Guangzhou, China (No. 201607020010), the China Postdoctoral Science Foundation (No. 2017M622681) and the Guangdong Natural Science Foundation (No. 2016A030310434) for their financial support. X.Z., and S.L., thank the National Natural Science Foundation of China (Grant No. 51727809) for its financial support.

## Conflict of Interest

The authors declare no conflict of interest.

## Keywords

non-fullerene acceptors, optical modeling, organic solar cells, space-charge effects, thick films

Received: May 25, 2018

Revised: June 14, 2018

Published online:

- [1] C. Yan, S. Barlow, Z. Wang, H. Yan, A. K. Y. Jen, S. R. Marder, X. Zhan, *Nat. Rev. Mater.* **2018**, *3*, 18003.
- [2] J. Hou, O. Inganäs, R. H. Friend, F. Gao, *Nat. Mater.* **2018**, *17*, 119.
- [3] G. Zhang, J. Zhao, P. C. Y. Chow, K. Jiang, J. Zhang, Z. Zhu, J. Zhang, F. Huang, H. Yan, *Chem. Rev.* **2018**, *118*, 3447.
- [4] Y. Lin, J. Wang, Z.-G. Zhang, H. Bai, Y. Li, D. Zhu, X. Zhan, *Adv. Mater.* **2015**, *27*, 1170.
- [5] F. Zhao, S. Dai, Y. Wu, Q. Zhang, J. Wang, L. Jiang, Q. Ling, Z. Wei, W. Ma, W. You, C. Wang, X. Zhan, *Adv. Mater.* **2017**, *29*, 1700144.
- [6] H. Bin, L. Gao, Z.-G. Zhang, Y. Yang, Y. Zhang, C. Zhang, S. Chen, L. Xue, C. Yang, M. Xiao, Y. Li, *Nat. Commun.* **2016**, *7*, 13651.

- [7] B. Fan, L. Ying, P. Zhu, F. Pan, F. Liu, J. Chen, F. Huang, Y. Cao, *Adv. Mater.* **2017**, *29*, 1703906.
- [8] S. Zhang, Y. Qin, J. Zhu, J. Hou, *Adv. Mater.* **2018**, *30*, 1800868.
- [9] W. Zhao, D. Qian, S. Zhang, S. Li, O. Inganäs, F. Gao, J. Hou, *Adv. Mater.* **2016**, *28*, 4734.
- [10] Y. Cui, H. Yao, C. Yang, S. Zhang, J. Hou, *Acta Polym. Sin.* **2017**, *5*, 135.
- [11] Z. Xiao, X. Jia, L. Ding, *Sci. Bull.* **2017**, *62*, 1562.
- [12] Z. Yamin, K. Bin, S. Yanna, W. Yanbo, X. Ruoxi, K. Xin, Y. Yuan-Qiu-Qiang, L. Chenxi, Y. Hin-Lap, W. Xiangjian, C. Yong, C. Yongsheng, *Adv. Mater.* **2018**, *30*, 1707508.
- [13] Y. Zhong, M. T. Trinh, R. Chen, G. E. Purdum, P. P. Khlyabich, M. Sezen, S. Oh, H. Zhu, B. Fowler, B. Zhang, W. Wang, C. Y. Nam, M. Y. Sfeir, C. T. Black, M. L. Steigerwald, Y. L. Loo, F. Ng, X. Y. Zhu, C. Nuckolls, *Nat. Commun.* **2015**, *6*, 8242.
- [14] Y. Guo, Y. Li, O. Awartani, H. Han, J. Zhao, H. Ade, H. Yan, D. Zhao, *Adv. Mater.* **2017**, *29*, 1700309.
- [15] D. Meng, H. Fu, C. Xiao, X. Meng, T. Winands, W. Ma, W. Wei, B. Fan, L. Huo, N. L. Doltsinis, Y. Li, Y. Sun, Z. Wang, *J. Am. Chem. Soc.* **2016**, *138*, 10184.
- [16] J. Liu, S. Chen, D. Qian, B. Gautam, G. Yang, J. Zhao, J. Bergqvist, F. Zhang, W. Ma, H. Ade, O. Inganäs, K. Gundogdu, F. Gao, H. Yan, *Nat. Energy* **2016**, *1*, 16089.
- [17] Z. Li, X. Xu, W. Zhang, X. Meng, W. Ma, A. Yartsev, O. Inganäs, M. R. Andersson, R. A. Janssen, E. Wang, *J. Am. Chem. Soc.* **2016**, *138*, 10935.
- [18] J. W. Jung, J. W. Jo, C.-C. Chueh, F. Liu, W. H. Jo, T. P. Russell, A. K. Y. Jen, *Adv. Mater.* **2015**, *27*, 3310.
- [19] Y. Lin, Z.-G. Zhang, H. Bai, J. Wang, Y. Yao, Y. Li, D. Zhu, X. Zhan, *Energy Environ. Sci.* **2015**, *8*, 610.
- [20] Y. Wu, H. Bai, Z. Wang, P. Cheng, S. Zhu, Y. Wang, W. Ma, X. Zhan, *Energy Environ. Sci.* **2015**, *8*, 3215.
- [21] S. Holliday, R. S. Ashraf, A. Wadsworth, D. Baran, S. A. Yousaf, C. B. Nielsen, C.-H. Tan, S. D. Dimitrov, Z. Shang, N. Gasparini, M. Alamoudi, F. Laquai, C. J. Brabec, A. Salleo, J. R. Durrant, I. McCulloch, *Nat. Commun.* **2016**, *7*, 11585.
- [22] W. Zhao, S. Li, H. Yao, S. Zhang, Y. Zhang, B. Yang, J. Hou, *J. Am. Chem. Soc.* **2017**, *139*, 7148.
- [23] Y. Yang, Z.-G. Zhang, H. Bin, S. Chen, L. Gao, L. Xue, C. Yang, Y. Li, *J. Am. Chem. Soc.* **2016**, *138*, 15011.
- [24] X. Xu, T. Yu, Z. Bi, W. Ma, Y. Li, Q. Peng, *Adv. Mater.* **2018**, *30*, 1703973.
- [25] S. J. Xu, Z. Zhou, W. Liu, Z. Zhang, F. Liu, H. Yan, X. Zhu, *Adv. Mater.* **2017**, *29*, 1704510.
- [26] B. Kan, J. Zhang, F. Liu, X. Wan, C. Li, X. Ke, Y. Wang, H. Feng, Y. Zhang, G. Long, R. H. Friend, A. A. Bakulin, Y. Chen, *Adv. Mater.* **2018**, *30*, 1704904.
- [27] Z. Luo, H. Bin, T. Liu, Z.-G. Zhang, Y. Yang, C. Zhong, B. Qiu, G. Li, W. Gao, D. Xie, K. Wu, Y. Sun, F. Liu, Y. Li, C. Yang, *Adv. Mater.* **2018**, *30*, 1706124.
- [28] J. Sun, X. Ma, Z. Zhang, J. Yu, J. Zhou, X. Yin, L. Yang, R. Geng, R. Zhu, F. Zhang, W. Tang, *Adv. Mater.* **2018**, *30*, 1707150.
- [29] Z. Fei, F. D. Eisner, X. Jiao, M. Azzouzi, J. A. Röhr, Y. Han, M. Shahid, A. S. R. Chesman, C. D. Easton, C. R. McNeill, T. D. Anthopoulos, J. Nelson, M. Heeney, *Adv. Mater.* **2018**, *30*, 1705209.
- [30] W. R. Mateker, M. D. McGehee, *Adv. Mater.* **2017**, *29*, 1603940.
- [31] C. Duan, F. Huang, Y. Cao, *Polym. Chem.* **2015**, *6*, 8081.
- [32] N. Gasparini, M. Salvador, T. Heumueller, M. Richter, A. Classen, S. Shrestha, G. J. Matt, S. Holliday, S. Strohm, H.-J. Egelhaaf, A. Wadsworth, D. Baran, I. McCulloch, C. J. Brabec, *Adv. Energy Mater.* **2017**, *7*, 1701561.
- [33] S. Feng, C. E. Zhang, Y. Liu, Z. Bi, Z. Zhang, X. Xu, W. Ma, Z. Bo, *Adv. Mater.* **2017**, *29*, 1703527.

- [34] Q. Fan, Y. Wang, M. Zhang, B. Wu, X. Guo, Y. Jiang, W. Li, B. Guo, C. Ye, W. Su, J. Fang, X. Ou, F. Liu, Z. Wei, T. C. Sum, T. P. Russell, Y. Li, *Adv. Mater.* **2018**, *30*, 1704546.
- [35] Y. Liu, J. Zhao, Z. Li, C. Mu, W. Ma, H. Hu, K. Jiang, H. Lin, H. Ade, H. Yan, *Nat. Commun.* **2014**, *5*, 5293.
- [36] H. Cha, J. Wu, A. Wadsworth, J. Nagitta, S. Limbu, S. Pont, Z. Li, J. Searle, M. F. Wyatt, D. Baran, J.-S. Kim, I. McCulloch, J. R. Durrant, *Adv. Mater.* **2017**, *29*, 1701156.
- [37] K. Sun, Z. Xiao, S. Lu, W. Zajaczkowski, W. Pisula, E. Hanssen, J. M. White, R. M. Williamson, J. Subbiah, J. Ouyang, A. B. Holmes, W. W. Wong, D. J. Jones, *Nat. Commun.* **2015**, *6*, 6013.
- [38] G. Zhang, K. Zhang, Q. Yin, X.-F. Jiang, Z. Wang, J. Xin, W. Ma, H. Yan, F. Huang, Y. Cao, *J. Am. Chem. Soc.* **2017**, *139*, 2387.
- [39] L. Lu, T. Xu, W. Chen, E. S. Landry, L. Yu, *Nat. Photonics* **2014**, *8*, 716.
- [40] S. R. Cowan, A. Roy, A. J. Heeger, *Phys. Rev. B* **2010**, *82*, 245207.
- [41] Y. Jin, Z. Chen, S. Dong, N. Zheng, L. Ying, X.-F. Jiang, F. Liu, F. Huang, Y. Cao, *Adv. Mater.* **2016**, *28*, 9811.
- [42] V. Mihailetschi, J. Wildeman, P. Blom, *Phys. Rev. Lett.* **2005**, *94*, 126602.
- [43] T. Kirchartz, T. Agostinelli, M. Campoy-Quiles, W. Gong, J. Nelson, *J. Phys. Chem. Lett.* **2012**, *3*, 3470.
- [44] K. Zhang, K. Gao, R. Xia, Z. Wu, C. Sun, J. Cao, L. Qian, W. Li, S. Liu, F. Huang, X. Peng, L. Ding, H.-L. Yip, Y. Cao, *Adv. Mater.* **2016**, *28*, 4817.
- [45] H. Shi, R. Xia, C. Sun, J. Xiao, Z. Wu, F. Huang, H. L. Yip, Y. Cao, *Adv. Energy Mater.* **2017**, *7*, 1701121.

# ADVANCED ENERGY MATERIALS

## Supporting Information

for *Adv. Energy Mater.*, DOI: 10.1002/aenm.201801609

Overcoming Space-Charge Effect for Efficient Thick-Film  
Non-Fullerene Organic Solar Cells

*Guichuan Zhang, Ruoxi Xia, Zhen Chen, Jingyang Xiao,  
Xuenan Zhao, Shiyuan Liu, Hin-Lap Yip,\* and Yong Cao*

## Supporting Information

## Overcoming Space-Charge Effect for Efficient Thick-Film Non-Fullerene Organic Solar Cell

Guichuan Zhang, Ruoxi Xia, Zhen Chen, Jingyang Xiao, Xuenan Zhao, Shiyuan Liu, Hin-Lap Yip,\* and Yong Cao

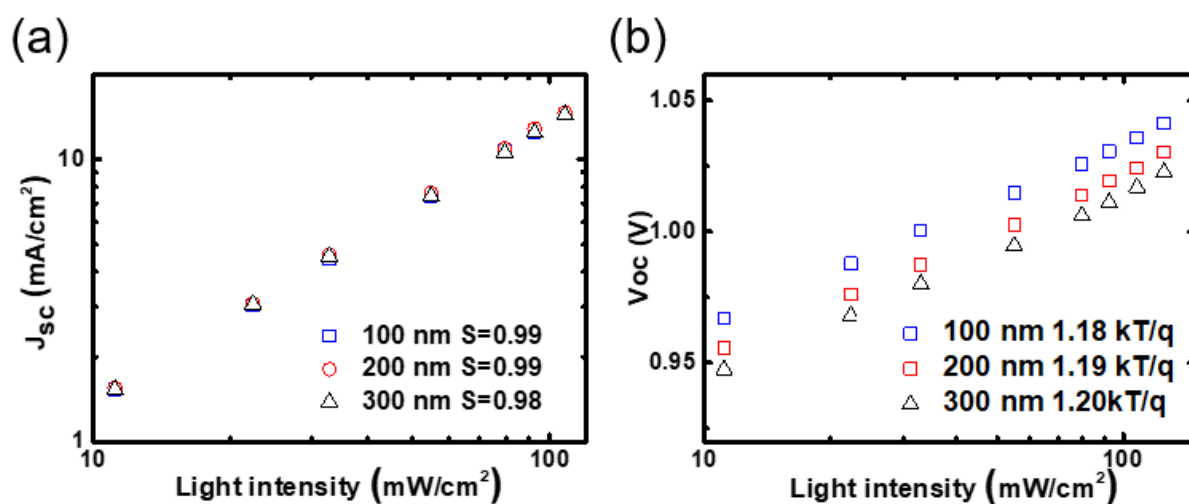


**Figure S1.** a)  $J_{sc}$  and b)  $V_{oc}$  versus light intensity characteristics of PffBT4T-2OD:EH-IDTBR-based OSCs with various active layer thicknesses using conventional device architecture.

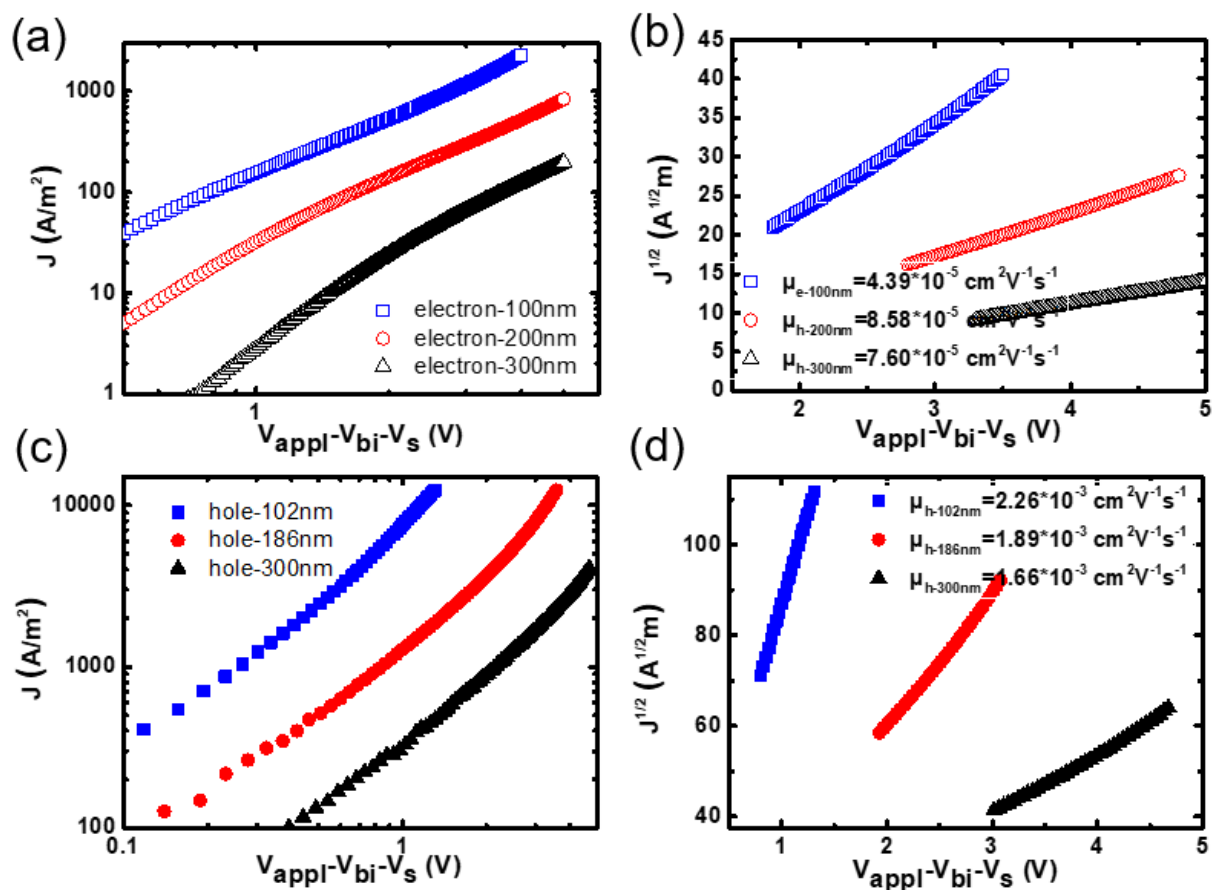


**Figure S2.**  $J$ ,  $J^{1/2}$  versus  $V_{\text{appl}} - V_{\text{bi}} - V_s$  characteristics of a), b) electron-only devices and c), d) hole-only devices with various active layer thicknesses.

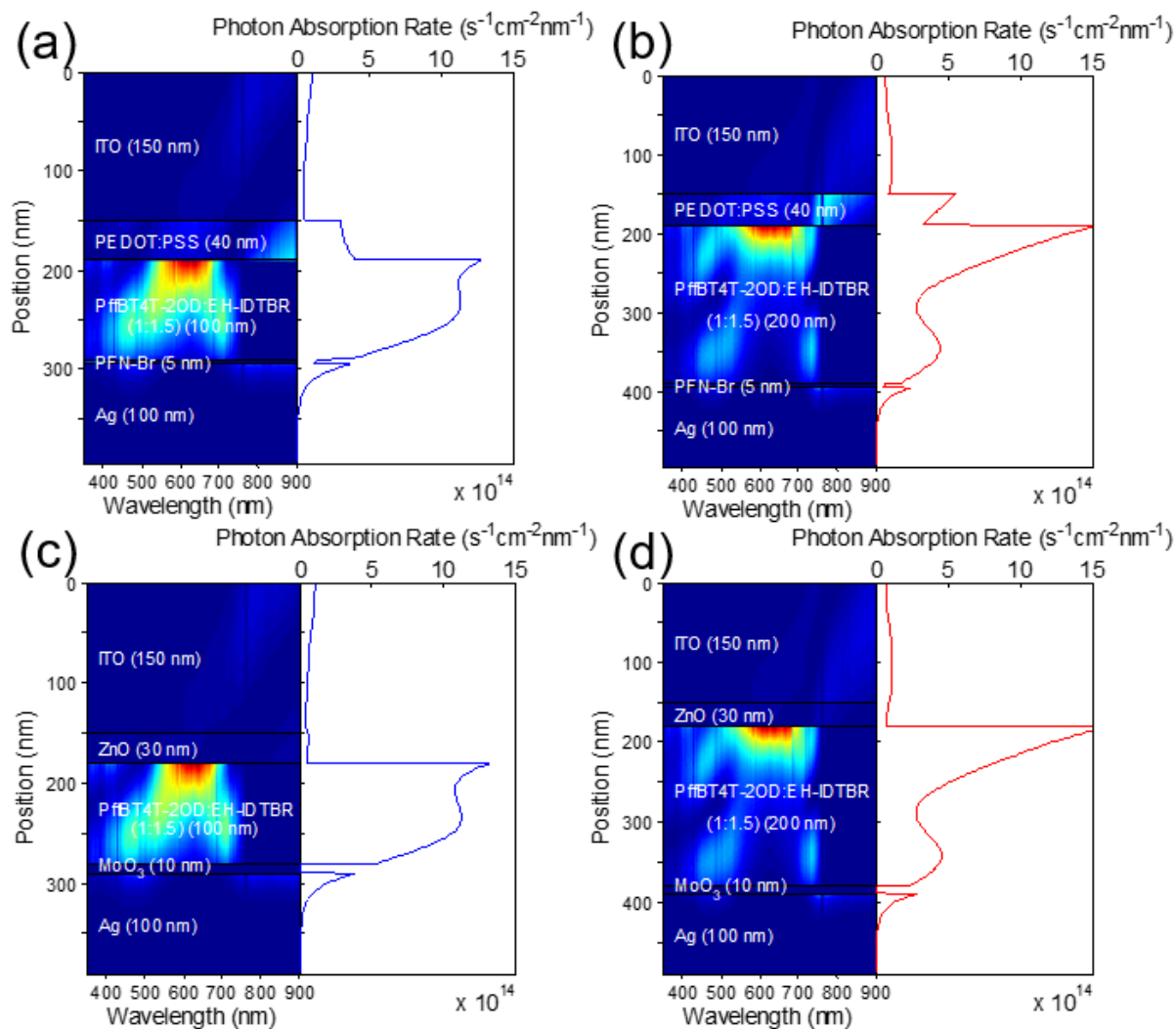


**Figure S3.** Simulated optical field distribution in PffBT4T-2OD:EH-IDTBR-based OSCs with active layer thicknesses of a), c) 100 nm and b), d) 200 nm using conventional and inverted device architecture, respectively.

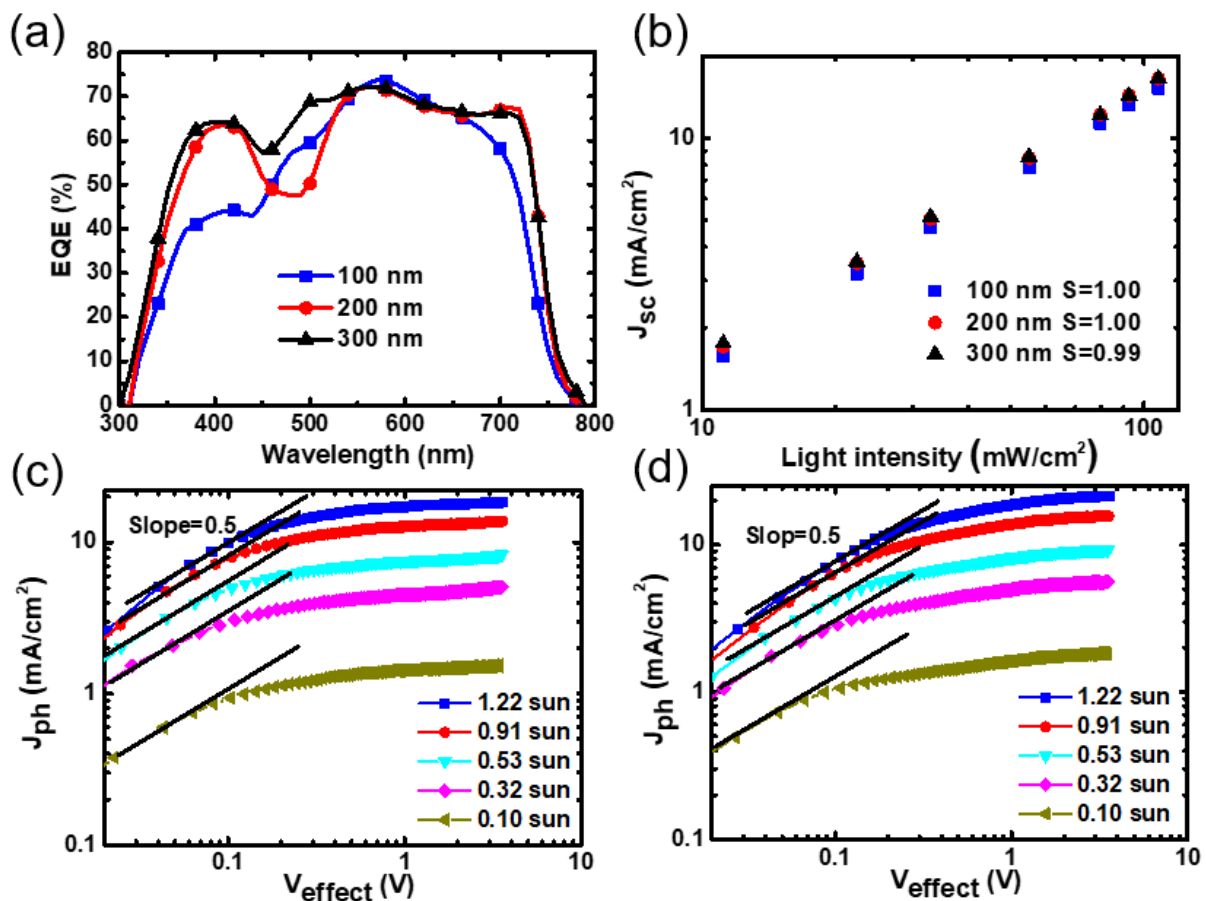


**Figure S4.** a) EQE spectra and b)  $J_{sc}$  versus light intensity characteristics of PffBT4T-2OD:EH-IDTBR-based OSCs with various active layer thickness using inverted device architecture.  $J_{ph}$  versus  $V_{effect}$  curves of inverted devices with active layer thicknesses of c) 100 nm and d) 300 nm.